Insights into the formation of the Cottonwood Canyon fault in the Catalina Schist

Justine G. Grabiec

Advisers: Sarah Penniston-Dorland, Richard Walker, & Melodie French

GEOL394: Final Report

Spring 2017

Abstract

Interpreting local structures and their role in a large scale system is important for understanding subduction zone and metamorphic processes. In the Catalina Schist of Santa Catalina Island, California, mélange associated with subduction zone processes consists of large blocks in a fine-grained matrix. This study seeks to shed light on the dynamic nature and possibly the formation of the mélange specifically on Catalina Island, as well as the relationship between the mélange and nearby units. This mélange is thought to have formed from the mixing of mafic and ultramafic protoliths, though the mixing processes themselves are poorly understood. On Catalina Island, the mélange shares a boundary with a coherent amphibolite unit. Within the coherent amphibolite and near this boundary is the Cottonwood Canyon fault with thicknesses ranging from 15-150 cm over a distance of only about 10 m and visible slickensides. Initial field observations indicated that the fault rock appeared mineralogically different from the host amphibolite. This observation brings into question the origin of the fault rock. The Cottonwood Canyon fault may demonstrate the dynamics of the formation of the mélange matrix as the fault rock may have been derived from the nearby incoherent mélange matrix, the coherent amphibolite hosting the fault, or a combination of both. A variety of geochemical and petrographic techniques were employed to test the hypothesis that the fault rock was in part derived from the mélange matrix. X-ray fluorescence was used to determine the major and trace element concentrations. Thermal ionization mass spectrometry was used to determine Os concentrations and $^{187}Os/^{188}Os$, ratios which are a measure of how much radiogenic Re was originally in the rock and from which an age of the rock can be calculated. Solution inductively coupled plasma mass spectrometry was used to determine other highly siderophile elements concentrations, including those of Re, Ru, Pt, Ir, and Pd. Electron probe microanalysis and petrography were used to determine the mineralogy of samples, and petrography was also used to identify deformation microstructures in the form of fractures, folds, kinked grains, and evidence of crystal lattice strain. X-ray diffraction was used to determine the mineralogy of fine-grained monomineralic fault rock samples. Geochemical heterogeneity and deformation microstructures in the fault imply that the fault experienced displacement both parallel and perpendicular to its boundaries, ultimately forming a fault rock with compositions intermediate between the coherent host amphibolite and mélange matrix. Furthermore, a possible chain of events is suggested for the fault formation that considers the mineralogy, deformation microstructures, and geochemistry of the fault and produces a system where mélange matrix flows into the fault during opening to mix with sheared amphibolite.

1. Introduction

The Catalina Schist is a metamorphic rock complex on Santa Catalina Island off of the coast of southern California, approximately 40 miles south of Los Angeles. The complex contains subduction-related metamorphic rocks that record the mechanisms and processes that took place during subduction and exhumation. This study investigates fault formation in the coherent amphibolite unit and nearby amphibolite facies mélange unit, which are part of the Catalina Schist (Fig. 1).

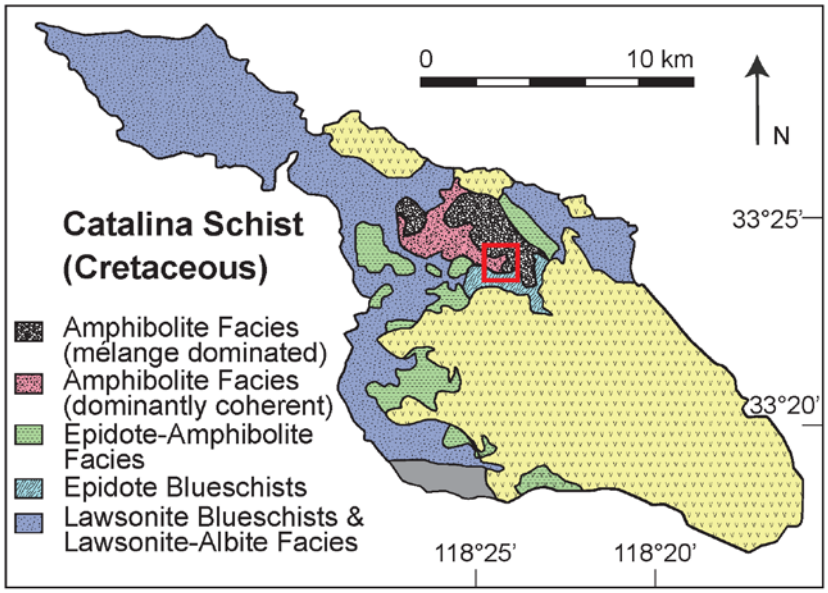

Fig. 1. The mélange dominated amphibolite facies rocks and dominantly coherent amphibolite facies (host rock) are the focus of this research. The red box indicates the location of the Cottonwood Canyon fault (adapted from Platt, 1975).

The Cottonwood Canyon fault occurs within the coherent amphibolite unit near its boundary with the mélange matrix. Upon initial observation, the rock within the fault appears mineralogically different from the amphibolite host rock. This discrepancy brings into question the origin of the fault rock as well as the nature of the formation of the fault. The hypothesis tested is that the fault rock was in part mechanically derived from the mélange matrix as opposed to solely derived from the coherent amphibolite either mechanically derived, chemically derived, or both. This research may provide insight into the formation of mélange matrix systems in general and specifically on Catalina Island, and may also shed light on the relationship between the coherent amphibolite unit and the mélange matrix on Catalina Island.

2. Geological Background

2.1 The Catalina Schist

The Catalina Schist consists of various amphibolite, blueschist, and lawsonite-albite facies rock units (Fig. 1). The coherent amphibolite and mélange-dominated amphibolite facies units are the focus of this study. The mélange contains mafic and ultramafic blocks in a fine-grained matrix containing talc, chlorite, amphiboles (anthophyllite and calcic-amphibole), and enstatite. Zircon, rutile, apatite, spinel, and Fe-Ni sulfides occur as minor phases (Bebout & Barton, 2002). The coherent amphibolite is a coarse-grained rock predominantly containing lineations of hornblende, and, to a lesser extent, plagioclase and epidote. Rutile and oxides are also variably present as minor phases in the coherent amphibolite. The pressures and temperatures of the Catalina Schist range from 7.5-11.5 kbar and 350-740 °C (Bebout, 2007). The amphibolite facies mélange experienced

pressures and temperatures of 8.5-11 kbar and 640-750 °C (Sorensen and Barton, 1987). Garnets and omphacite from a hornblende eclogite were analyzed for Lu and Hf isotopes and resulted in calculated rock ages of 114.5 ± 0.6 Ma (Anczkiewicz et al., 2004).

2.2 The Mélange Matrix

The mélange matrix is thought to have formed through tectonic mixing processes and metasomatic alteration of mafic and ultramafic blocks (Bebout & Barton, 2002), as illustrated in Fig. 2. Evidence suggesting fluid infiltration of the system was documented by Sorensen and Barton (1987), Bebout and Barton (1989), and others. As aqueous fluids infiltrated the system, metasomatism altered the outer edges of the blocks. Petrological and geochemical analysis of Ca- and Mg-rich and Na- and Al-poor clinopyroxenes, garnets, and amphiboles performed by Sorensen (1988) and Sorensen and Grossman (1989) indicated that the altered rims, or "rinds," formed during geochemical exchange. Some rinds and mélange matrix also contain abundant amounts of anthophyllite, talc, and quartz representative of a system reaching about 750˚C (Sorensen and Barton, 1987). The rinds flaked off in a continuous process over a range of depths during subduction as documented by Sorensen (1988) and Penniston-Dorland et al. (2014). Accumulation of these flakes formed the incoherent mélange matrix unit with a composition intermediate between mafic and ultramafic (Bebout and Barton, 2002). Sorensen (1988) also found that some of the mafic blocks experienced some degree of migmitization.

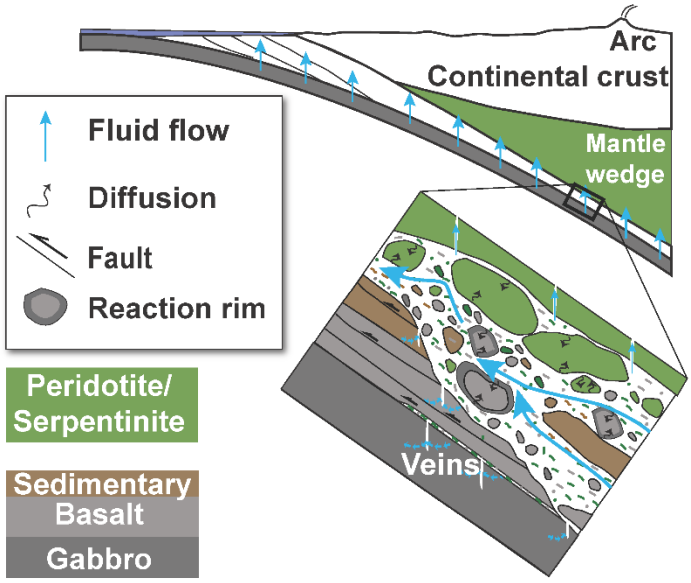

Fig. 2. Formation of the mélange matrix as mafic and ultramafic blocks are tectonically and metasomatically altered (Bebout & Penniston-Dorland, 2016).

Fig. 3. Slickensides observed in the field.

3. Fault

The Cottonwood Canyon fault is a steeply dipping fault with variable in thickness and mineralogy. Displacement is apparent in slickensides (Fig 3). The thickness corresponds to a relatively fine-grained fault core which is surrounded by a coarser-grained damage zone on either

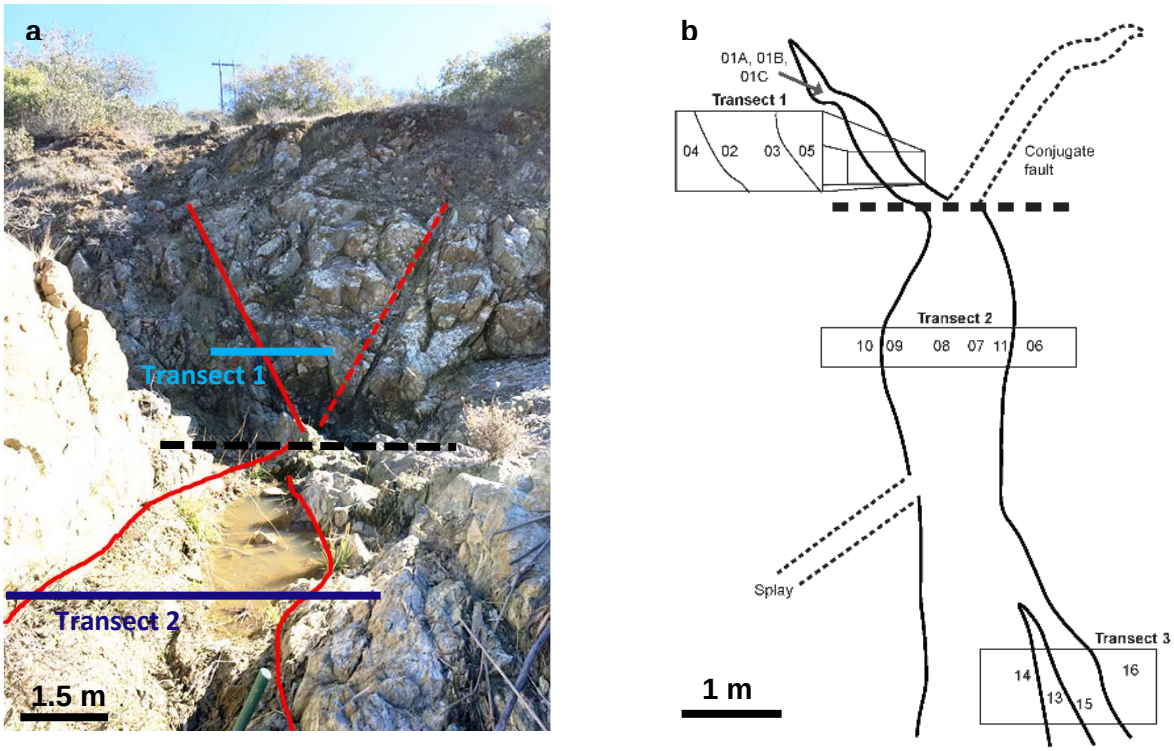

Fig. 4. a) The vertical wall contains the thinnest portion of the exposed fault core and part of the middle of the exposed fault that contains the thicker portion of the fault core. The solid red line marks the studied fault. The dashed red line marks a possible conjugate fault that is not be a focus of the study but is still an interesting feature nevertheless. b) This outline of the fault displays the three transects as well as the possible conjugate fault and a potential splay of the fault. The numbers represent the location of sample collection, all of which are labeled with the prefix "A16-" followed by the number and letter combination found above. Sample A16-12 is not pictured, as it was collected 64m away from the fault. The horizontal, bold, black dashed line is located on the same area of the fault in each image.

side within the host amphibolite, both of which are characteristic of faults as described by Chester et al. (1993) and Shipton et al. (2006). Thickness measurements of the exposed fault core vary from 15 cm (transect 1, Fig. 4) to 1.5 m (transect 3, Fig. 4) over a distance of about 10 m. Although not part of the study, a steeply dipping conjugate fault is apparent near the thin portion of the main fault and a potential splay of the fault is located in the thicker portion of the main fault (Fig. 4). Fault rock in the thin portion is loose, semi-cohesive, and distinctly green in color. The mineralogy is more variable in the thicker portions of the fault core and lacks the distinctive green color characteristic of the transect 1 fault rocks, but is still semi-cohesive. The host amphibolite is cohesive, more resistant to weathering than the fault rock, and a medium grey throughout the outcrop. The host amphibolite is also more visibly fractured in the damage zone than in the distal portions of the unit.

4. Samples

Eighteen samples were collected throughout three transects along the fault – one across the thin portion, a second across the middle of the exposure, and a third across the widest portion of the fault – from which 16 samples were made into thin sections. In total, five samples collected are of the host amphibolite; four were within a meter of the fault whereas a fifth (A16-12) was collected

64 meters away. The other 13 samples collected are fault rock. Billets for all samples except A16-01A and -11 were cut and sent to Spectrum Petrographic Incorporated to make thin sections 30 μm thick. Twelve samples – three host amphibolite and nine fault rock - were crushed into fine powders.

5. Analytical Methods

5.1 Petrography

Thin sections were examined to determine mineralogy and classify deformation microstructures. The microscope used was a Nikon Eclipse LV1000POL and minerals were identified based on their optical properties in transmitted light.

5.2 XRF

The samples analyzed via X-ray fluorescence (XRF) for major and trace elements were sent to Franklin & Marshall College who used a PANalytical 2404 X-ray fluorescence vacuum spectrometer, a PW2540 X-Y sample handler, and 4KW Rh super sharp X-ray tube. Relative standard deviation (RSD) for major elements is <0.6%. For trace elements with concentrations above 25 ppm, the RSD is <5%, except for that of Cr, which is 13%. Trace elements with concentrations lower than 25 ppm have RSDs less than 35%. Loss on ignition (LOI) was first determined by heating a specific amount of a sample for an hour at 950°C. Major element concentrations were determined by creating a glass disk with a flat surface from molten sample. X-rays then interacted with a flat side of this disk; it was from these interactions that the major element concentrations were determined. Trace element concentrations were determined from sample briquettes formed by applying a considerable amount of pressure (50,000 psi) to the powdered samples. The methods followed and standards used are those outlined by Penniston-Dorland et al. (2014).

5.3 XRD

Three samples from transect 2 were powdered to a grain size less than 0.074 mm and sent to the Department of Chemistry at the University of Maryland for X-ray diffraction (XRD) analysis. The samples weighed between 0.1 and 0.2 g. Instruments used were the C2 Discover with 2D detector and the D8 Advance with LynxEye and SolX. The two theta range was 5-90° and each sample was scanned for one hour.

5.4 EPMA

The instrument used for electron probe microanalysis (EPMA) was a JXA-8900 SuperProbe, a high resolution scanning electron microscope and wavelength-dispersive/energy-dispersive combined electron probe microanalyzer. Both wavelength-dispersive spectrometry (WDS) and energy-dispersive spectrometry (EDS) data were collected. The probe current used during the EDS analysis was 25.06 nA and the beam had a voltage of 15.0 keV. The beam size ranged between 1 and 100 μm, and was adjusted accordingly to avoid any mineral inclusions. During WDS analysis, the accelerating voltage was 15 kV, the sample current was 20 nA, and the beam diameter was 10 μm.

5.5 HSE Geochemistry

Highly siderophile elements (HSEs), including Os, Re, Ru, Pt, Ir, and Pd, were concentrated in trace alloys and sulfides found in the sample. These phases were dissolved with aqua regia, a mixture of HCl and HNO_3, in sealed Carious tubes at 240 °C in an oven in order to measure the concentration of the HSEs and $^{187}Os/^{188}Os$ ratios of each sample. A blank was also analyzed to determine how much of each HSE were contributed to the sample from non-sample sources (i.e. spikes).

Osmium can be oxidized to its highest valence state of +8 with spikes enriched with isotopes of Os and the other highly siderophile elements (HSEs) to make Os easily separable from the rest of a given sample. The spikes added to the analyzed samples are enriched with ^{185}Re, ^{190}Os, ^{191}Ir, ^{99}Ru, ^{195}Pt, and ^{105}Pd. The HSE separation methods closely follow those of Becker et al. (2001) and Becker et al. (2006). Osmium was chemically separated from the rest of the HSEs, at which point the rest of the HSEs were further separated via column chemistry and chromatography. A more detailed overview of the geochemical separation methods can be found in Appendix I. The concentrations of Os and the $^{187}Os/^{188}Os$ ratios were determined using a Thermo Fisher Triton thermal ionization mass spectrometer (TIMS). Various other HSE isotope ratios for Re, Ir, Ru, Pt, and Pd were determined using a Nu Plasma multi-collector inductively coupled plasmas mass spectrometer (ICP-MS) from which the concentrations were calculated.

6. Results

6.1 Mineral Assemblages

Samples from transect 1 consist mainly of randomly oriented pumpellyite (Fig. 6) and hornblende. The hornblende is likely physically derived from the host amphibolite as the grains in the fault rock are similar in shape and size to those of the host amphibolite. Though minor, there is a yellow material that was unable to be identified during the course of the research. Back scatter electron (BSE) imaging and EDS spectra can be found in Fig. 8.

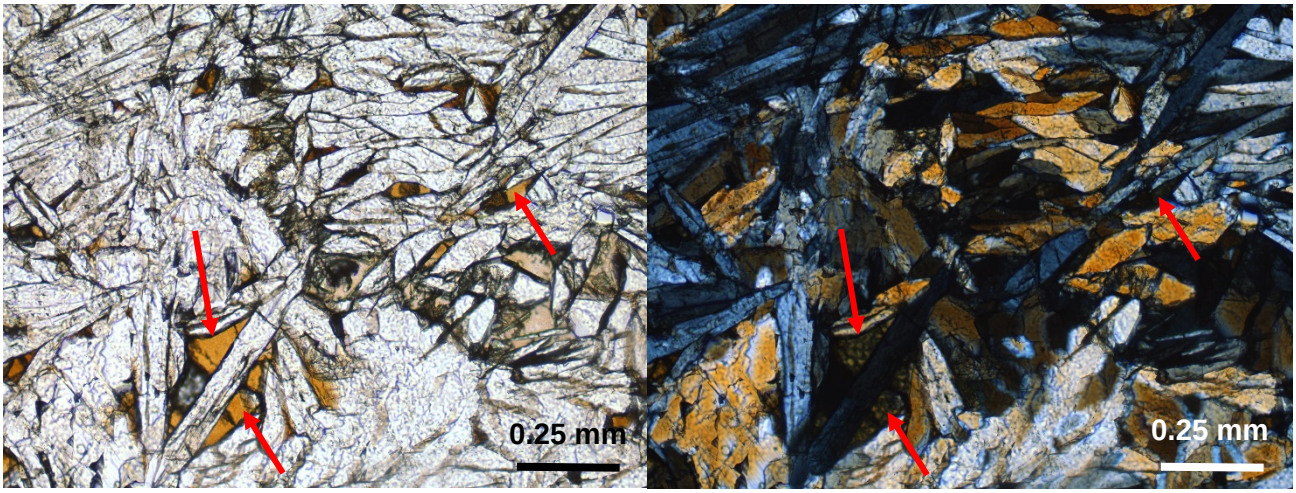

Fig. 5. Sample A16-01B consists mostly of pumpellyite, though an unknown yellow material is also present. The red arrows are pointing at this yellow material. The pumpellyite is colorless in plane polarized light (PPL; left) and first order black to first order yellow in cross polarized light (XPL; right).

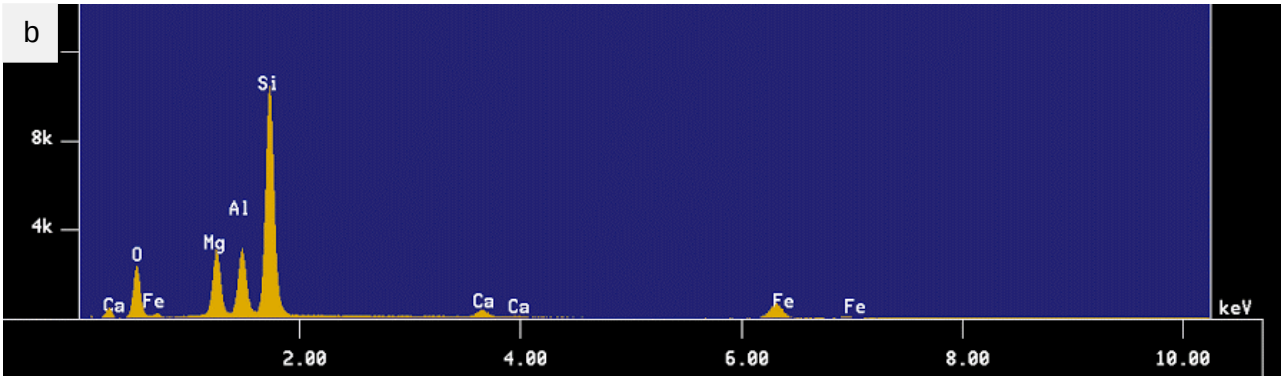

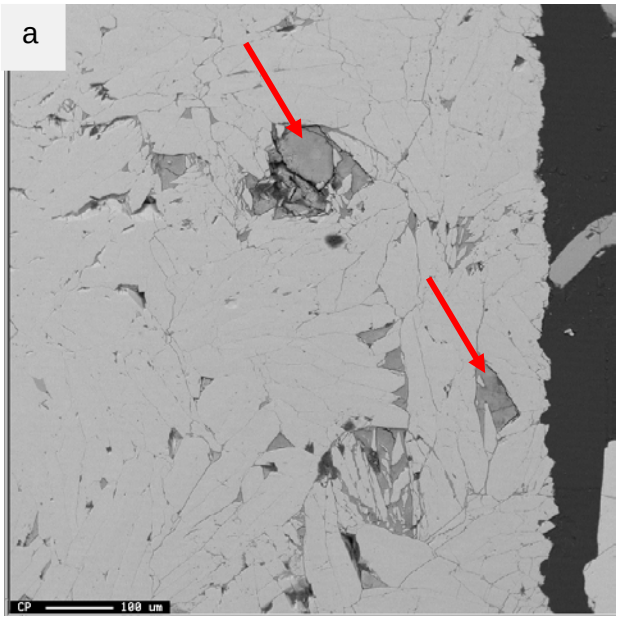

Fig. 6. Both images were captured via EPMA. a) BSE image of sample A16-01B. The relatively brighter minerals are pumpellyite and the less bright minerals are the yellow material (indicated by red arrows). Changes in brightness within and among the yellow material grains indicate that the grains are not homogenous. b) Energy dispersive spectroscopy spectra of a yellow material target (not pictured).

The mineralogy of samples from transect 2 contains far more hornblende and chlorite and less pumpellyite than transect 1. A coherent amphibolite sample (A16-10) containing primarily hornblende, however, shows evidence of extremely altered hornblende with nearby pumpellyite (Fig. 7). Samples from transect 2 contain pumpellyite and amphiboles as monomineralic fault material made evident by XRD analysis (see Appendix III for collected spectra). The magnesiohornblende and pumpellyite were unconsolidated while the actinolite was consolidated. The mineralogy of transect 3 is dominated by chlorite and epidote. A more complete description of hand specimens and thin sections can be found in Appendix II.

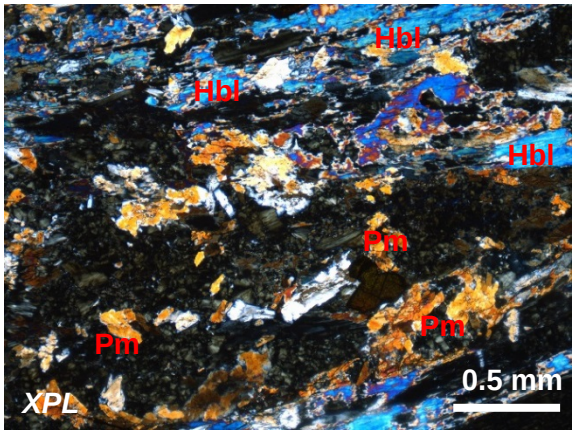

Fig. 7. Sample A16-10, a coherent amphibolite sample from transect 2 with extremely altered hornblende and nearby pumpellyite grains.

6.2 Deformation Microstructures

The deformation microstructures of transect 2 are the focus of this study because transect 2 is the most representative of both the host amphibolite and fault rock. Predominant microstructures in the fault rock include folding of the fine-grained chlorite and hornblende with transgranular and intragranular fractures within the larger hornblende grains. Folding is more apparent on the right side of transect 2 whereas

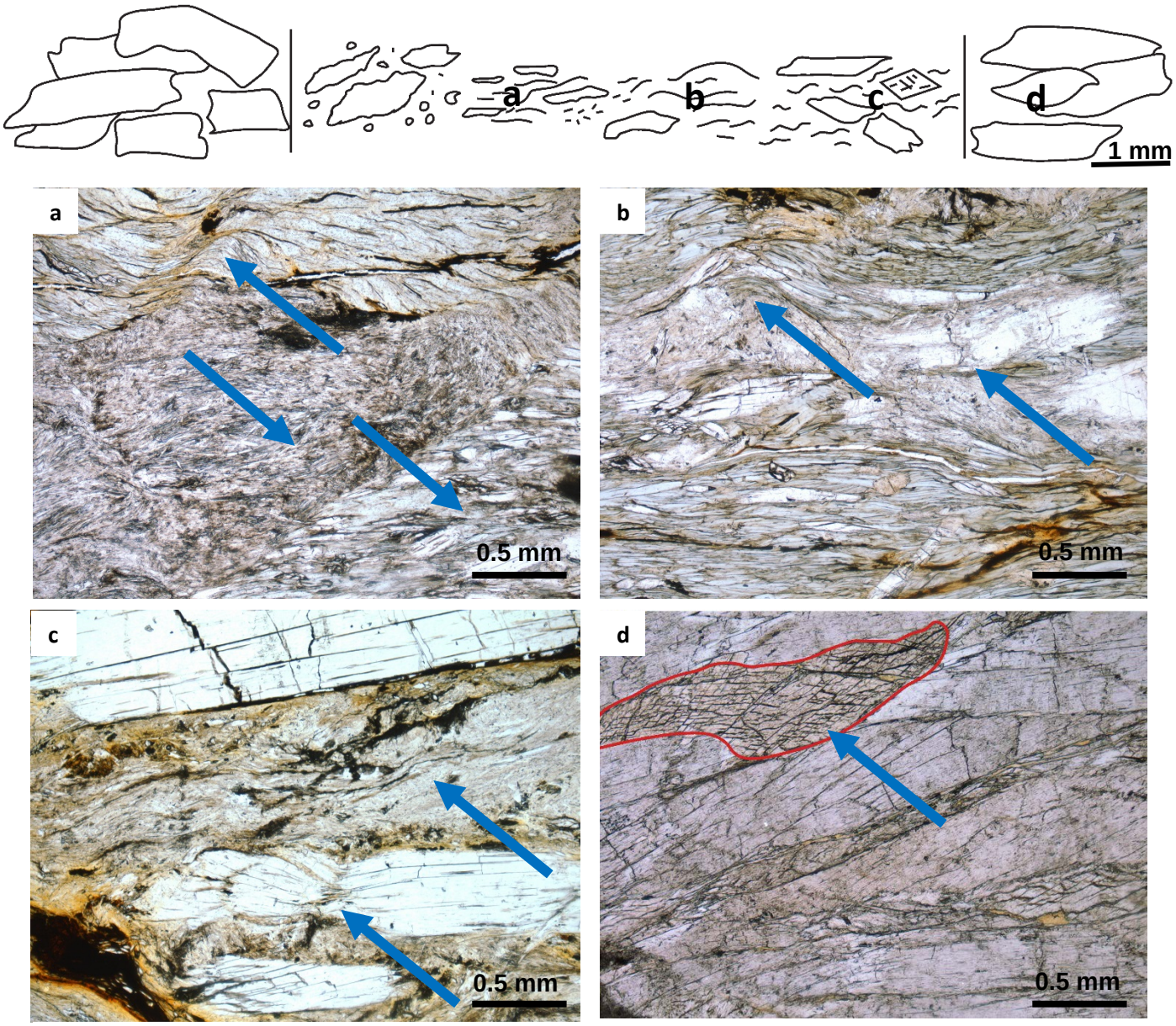

Fig. 8. Deformation microstructures across transect 2 with corresponding images a, b, c, and d in PPL. Vertical lines represent the boundaries of the fault, closed angular polygons represent hornblende grains, small, closed, rounded shapes represent abundance fine-grained quartz, lines enclosed in shapes represent cleavage, and lines outside of shapes represent folding. a) Fault rock with zones marked by different grain sizes and microstructures which include folding. Minerals include fine-grained chlorite and hornblende. b) Fault rock with fine-grained chlorite and coarse-grained hornblende with folding and a fractured grain. c) Fault rock with folds in fine-grained chlorite and large hornblende grains, some of which are pinched. d) Coherent amphibolite dominated by hornblende with hornblende boudins outlined in red.

alteration is more characteristic of the left side of the transect 2 fault rock, though fractures are found throughout transect 2. Deformation microstructures within and among host amphibolite grains occur as fractures or boudins, and are less extensive in the host amphibolite as compared to the fault rock.

A qualitative description of the deformation microstructures in transect 2 is presented in Fig. 8. On the left side of transect 2, folding is present in both chlorite and hornblende but less predominant in the hornblende grains, which are small and subhedral (Fig. 8a). Towards the center of the fault, folding becomes more predominant in larger subhedral hornblende grains, and is still common among fine-grained chlorite (Fig. 8b). Further to the right, the chlorite in the fault rock contains significant folding among fine-grained chlorite, though large subhedral to euhedral hornblende grains are intensely fractured and pinched (Fig. 8c). The host amphibolite in the damage zone contains euhedral amphibolite grains or hornblende boudins with a high fracture density (Fig. 8d). Distal host amphibolite contains few deformation microstructures within and among euhedral hornblende grains. A more detailed description of deformation microstructures in each sample can be found in Appendix II.

6.3 XRF

Specimen	T1 Fault A16-01B	T1 Fault A16-02	T1 Fault A16-03B	T2 Host A16-06	T2 Fault A16-07	T2 Fault A16-08	T2 Fault A16-09	T2 Host A16-10	Host* A16-12	T3 Fault A16-13	T3 Fault A16-14	T3 Fault A16-15
SiO_2	40.61	42.25	46.68	50.33	54.70	51.84	51.93	42.56	45.03	50.37	53.66	46.86
TiO_2	0.05	1.16	0.66	0.27	0.00	0.09	0.45	1.45	0.32	0.09	0.04	0.16
Al_2O_3	27.46	15.70	13.10	9.55	2.19	4.48	15.47	14.54	18.32	5.24	3.33	17.98
Fe_2O_3	3.08	14.74	9.93	8.51	8.42	9.93	9.44	15.30	7.15	11.95	9.81	5.29
MnO	0.19	0.19	0.15	0.16	0.25	0.15	0.17	0.22	0.13	0.17	0.14	0.10
MgO	4.13	13.58	14.24	16.84	22.36	23.13	10.96	15.09	11.06	23.06	21.73	10.75
CaO	23.88	10.90	13.93	11.98	11.43	9.98	6.68	9.25	15.95	8.60	11.00	17.04
Na_2O	0.25	0.88	0.94	1.81	0.33	0.27	4.33	1.22	1.64	0.25	0.24	1.07
K_2O	0.000	0.051	0.098	0.267	0.024	0.016	0.382	0.121	0.153	0.012	0.019	0.295
P_2O_5	0.003	0.218	0.024	0.004	0.007	0.001	0.008	0.007	0.011	0.003	0.002	0.007
Total	**99.653**	**99.669**	**99.752**	**99.721**	**99.711**	**99.887**	**99.820**	**99.758**	**99.764**	**99.745**	**99.971**	**99.552**
LOI	7.11	4.78	4.99	1.46	2.80	4.42	2.76	4.86	0.78	6.14	3.66	1.06
Rb	1.2	<0.5	0.5	3.5	<0.5	<0.5	8.8	1.7	1.8	<0.5	<0.5	6.4
Sr	5	197	14	26	10	9	130	26	274	7	6	235
Y	4.4	75.7	24.8	9.0	9.7	5.9	61.3	74.5	15.4	3.1	3.8	13.9
Zr	11	273	26	14	10	10	141	139	22	11	10	14
V	181	357	157	160	33	75	185	301	174	63	49	124
Ni	102	332	352	487	630	672	202	388	209	1057	763	207
Cr	128	574	737	1460	1675	2435	526	1165	478	2376	1053	651
Nb	<0.5	10.1	0.7	<0.5	<0.5	<0.5	1.0	11.4	<0.5	<0.5	<0.5	<0.5
Ga	15.0	16.1	10.2	8.0	3.5	7.5	11.1	12.5	12.9	7.6	5.6	14.0
Cu	31	209	180	40	624	168	146	201	63	123	101	51
Zn	28	118	64	49	64	63	85	147	48	67	62	37
Co	4	56	57	59	51	64	31	64	42	100	50	31
Ba	20	15	22	165	<3	16	393	61	82	9	5	136
La	12	17	8	9	8	6	22	9	8	8	6	10
Ce	9	46	11	9	6	5	55	17	13	3	10	12
U	<0.5	1.5	<0.5	<0.5	<0.5	<0.5	<0.5	<0.5	0.5	<0.5	<0.5	<0.5
Th	<0.5	15.4	<0.5	<0.5	<0.5	<0.5	13.2	4.0	<0.5	1.0	<0.5	<0.5
Sc	21	38	53	44	10	15	27	33	43	12	16	46
Pb	10	<1	3	<1	<1	<1	<1	<1	<1	<1	<1	1

Table 1. XRF data collected at Franklin & Marshall College. T1, T2, and T3 refer to transects 1, 2, and 3 respectively, as illustrated in Fig. 2. Major elements are reported as oxides in weight percent and trace elements are reported in parts per million. *Sample A16-12 is not part of a transect as it was collected 64 m away from the fault.

The XRF data for the twelve powdered samples are summarized in Table 1. As compatible elements, Ni and Cr will be higher in ultramfic rocks compared to mafic rocks, and high MgO is

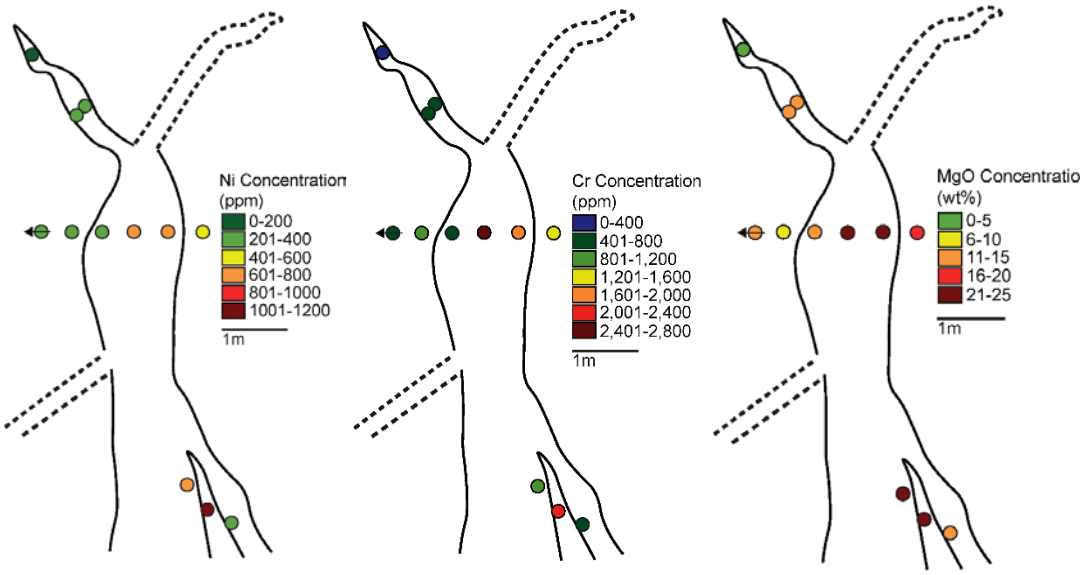

Fig. 9. Maps of fault outline, sample locations, and corresponding Ni, Cr, and MgO concentrations of each sample. The sample with an arrow refers to sample A16-12 collected 64 m away from the fault.

also generally associated with ultramafic rocks. Figure 9 shows XRF data for Ni, Cr, and MgO concentrations in and around the fault across transect 2. The concentrations of these elements are higher in the fault rock and also in some of the amphibolite samples adjacent to the fault and in the damage zone than in the distal host amphibolite.

6.4 HSE Concentrations and $^{187}Os/^{188}Os$ Ratios

Osmium, Ir, Ru, Pt, Pd, and Re concentrations are presented in Table 2. These concentrations are plotted as primitive upper mantle normalized values to be compared to previously analyzed of samples of the cores, rinds, and mélange (Fig. 11) by Penniston-Dorland et al. (2012). The distal host amphibolite (sample A16-12) is consistent with having a basaltic protolith. The other host amphibolite sample collected near the fault (A16-06) is similar to the mélange and had a peridotitic protolith according to its HSE geochemistry. The two fault samples (A16-08, A16-09) are also geochemically similar to the mélange which again implies it had a peridotitic protolith.

a)	MgO (wt%)	Cr (ppm)	Ni (ppm)	Os (ppb)	Ir (ppb)	Ru (ppb)	Pt (ppb)	Pd (ppb)	Re (ppb)	b)	$^{187}Os/^{188}Os$	$^{187}Re/^{188}Os$	$^{187}Os/^{188}Os_{initial}$
A16-06	16.84	1460	487	2.36	1.64	2.27	30.8	2.65	0.0051		0.166	0.011	0.17
Uncertainty (%)	0.101	190.	24.3	0.0032	0.031	2.03	0.076	3.23	100*		0.107	100*	<0.001
A16-08	23.13	23.13	672	0.963	--	1.30	--	2.30	0.0686		0.152	0.34	0.15
Uncertainty (%)	0.139	316.5	33.6	0.0079	--	7.06	--	7.42	7.41		0.161	7.4	<0.001
A16-09	10.96	526	202	0.558	0.285	1.00	15.2	1.28	0.595		0.225	5.2	0.22
Uncertainty (%)	0.0658	68.3	10.1	0.0137	0.35	9.16	0.309	13.2	0.854		0.122	0.85	0.046
A16-12	11.06	478	209	0.007	0.00093	0.0043	0.16	0.28	0.0058		0.382	4.2	0.37
Uncertainty (%)	0.0664	62.1	10.5	0.12	12	44	52	3.0	6.2		0.273	6.3	0.16

Table 2. a) The concentrations of the HSEs and their uncertainties with XRF data for MgO, Cr, and Ni for comparison. b) Various Os and Re isotope ratios that can be used to calculate the ages of the rocks. Uncertainty descriptions can be found in Appendix II. *Uncertainties of 100% are attributed to samples depleted in Re where most Re contributed to the sample originated from the spike; these high uncertainties do not affect the overall conclusions of the study.

7. Discussion

In general, there are three different fracture forming kinematics: mode one (opening) and modes two and three (shearing), which will be combined for simplicity. Faults are a subset of fractures and are formed by shearing. The presence of slickensides and the fact that the fault has a fault core implies that the fault formed from shearing; while shearing can contribute to a fault core, variable thickness in the fault core is attributed to opening. Thus, the fault core likely formed by some combination of these mechanisms, such as opening followed by shearing, shearing followed by opening, or by contemporaneous opening and shearing (mixed mode). A damage zone surrounding the fault core formed contemporaneously with the fault. The damage zone in the host amphibolite differs from the distal host amphibolite by not only having more factures and boudins, but also by heightened concentrations of Ni, Cr, MgO, and HSEs (Figs. 11 & 12) which may have been derived chemically from the fault rock. Thus, chemical signatures of increased Ni, Cr, MgO, and HSEs may be a result of either physical mixing in the fault core or by a fluid-mediated process such as diffusion or mass transport by an advecting fluid.

Nickel, Cr, and the HSEs are not generally considered to be fluid-mobile elements, as noted by Bebout and Barton (2002) and Penniston-Dorland et al. (2012), but the possibility that they are fluid-mobile in this context cannot be excluded. Boudins and fractures are present among hornblende grains in the damage zone, as are altered hornblende grains which share grain boundaries with pumpellyite grains (Fig. 7). The alteration of hornblende to pumpellyite suggests that there might have been a fluid-mediated reaction at some point.

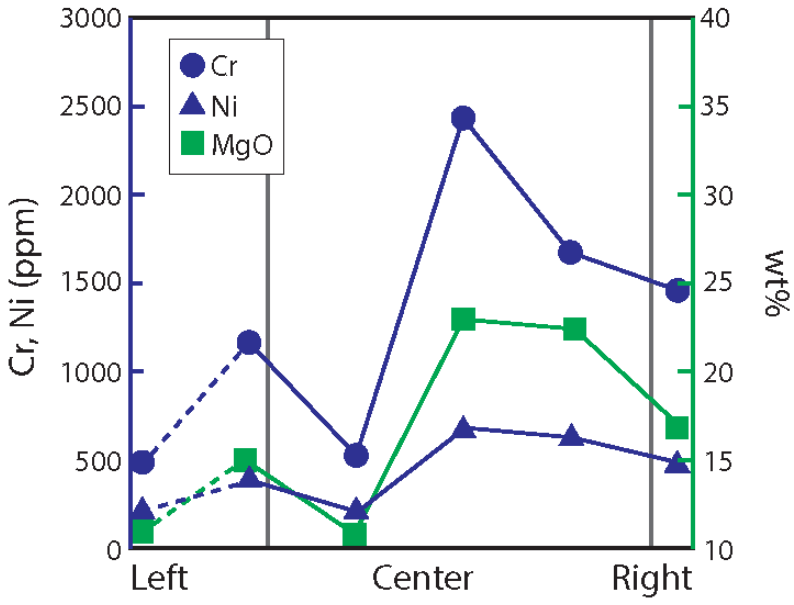

Fig. 10. The concentrations of Ni and Cr were measured in ppm while MgO was measure in wt%. The x-axis refers to location in the field relative to the fault. The dashed line implies that the sample furthest to the left was collected 64 meters away from the fault whereas the other two host samples were collected on either side of the fault. The grey lines represent the boundaries between the fault rock (inside the grey lines) and the host amphibolite (outside the grey lines).

Geochemical and petrologic data, combined with previous work, indicate that some sort of mixing occurred to form the fault rock. Magnesium, Ni, Cr, and Os are all enriched in the mélange matrix relative to amphibolite blocks in the mélange (Penniston-Dorland et al., 2012), and thus likely enriched relative to the host amphibolite as well. Furthermore, rind HSE patterns that formed the mélange matrix are similar to those of peridotites (Penniston-Dorland et al., 2012). Evidence for mixing of mafic and ultramafic material is implied by the heterogeneity of the geochemistry of transect 2. More specifically, the Cr, Ni, and MgO concentrations are variable within the fault and higher than the distal

amphibolite (Fig. 10). Furthermore, higher concentrations of HSEs (in particular, Os, Ir, and Ru) in the fault and damage zone as compared to host rock 64 m away from the fault indicate that some fault material likely originated from the mélange matrix (Fig. 11). Similar geochemical characteristics between the fault rock and host amphibolite would imply that the fault rock simply originated from the host amphibolite. There is geochemical evidence for an ultramafic source contributing to the heterogeneity of the fault rock because the fault rocks and damage zone amphibolite HSE concentrations are similar to those of peridotites as opposed to basalts. Thus, it is likely the mélange matrix contributed some ultramafic material to the fault rock.

Fault rock concentrations of Ni, Cr, and MgO are in between those of mafic endmember averages and mélange matrix (Fig. 12). Since the fault rock has low concentrations of these elements, it is not solely derived from the mélange matrix and instead must contain some additional mafic component, which is consistent with mélange matrix having mixed with sheared host amphibolite.

Pumpellyite within transect 1 does not have a shape preferred orientation, which implies that there has not been any differential crystallographic strain since the pumpellyite crystallized. Thus, the pumpellyite crystals are likely post-tectonic (Fig. 5). Chlorite and amphibole in transect 2 show obvious evidence of strain as kinks, folds, and fractures (Fig. 9), making these crystals pre- or syn-tectonic and they would have crystallized prior to the

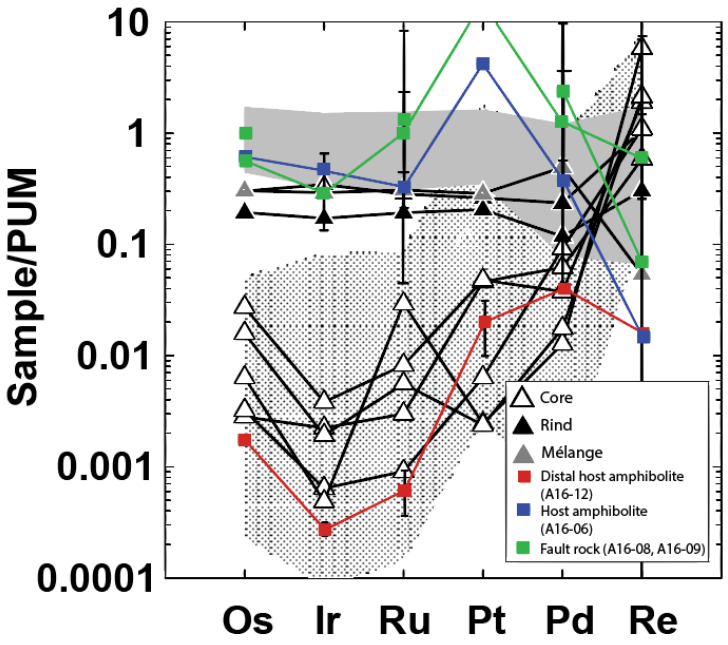

Fig. 11. HSE concentrations normalized to the primitive upper mantle (PUM) values determined by Becker et al. (2006) discriminate between ultramafic and mafic rocks. Triangles represent data from Penniston-Dorland et al. (2012). The crosshatched zone is the area where basalts plot; the solid grey zone is the area where peridotites plot.

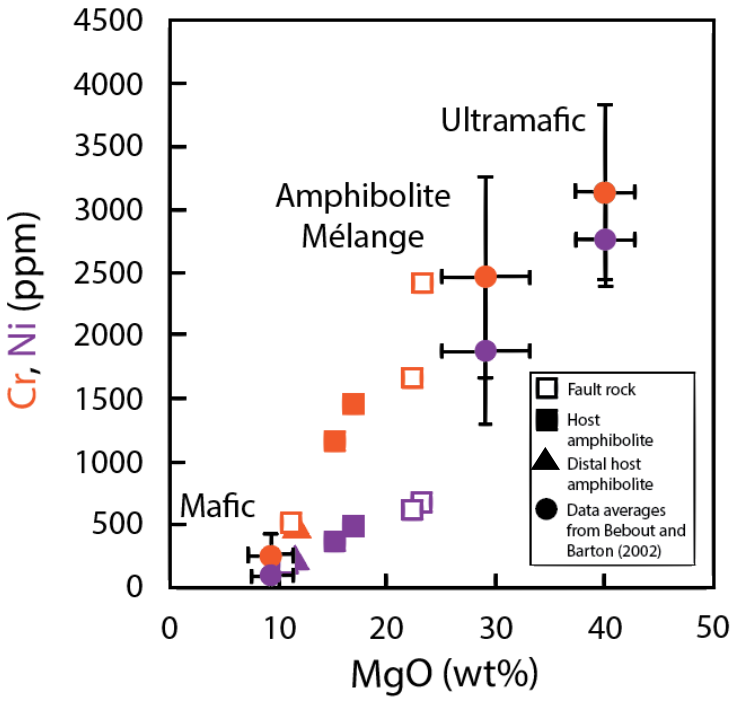

Fig. 12. MgO, Cr, and Ni concentrations in fault rock and host amphibolite as compared to mafic and ultramafic endmember averages as well as mélange matrix concentrations collected by Bebout and Barton (2002).

pumpellyite under higher pressure and temperature conditions. The mélange unit crystalized at 0.8-1.1 GPa and 640-750 °C (Bebout and Barton, 2002); the coherent amphibolite unit likely crystallized at similar pressures and temperatures as both are amphibolite-grade. Pumpellyite crystallizes at relatively low pressures and temperatures, and therefore likely formed during exhumation of the fault. Liou et al. (1985) report pumpellyite crystallization around 0.08-0.45 GPa and 140-325 °C. There is also evidence for hornblende alteration to pumpellyite (Fig. 6), which is direct evidence for retrograde metamorphism. Mineral reactions in mafic rocks involving pumpellyite have not been well studied. Possible reactions include Eq. 1 suggested by Brown (1977), a generalized, non-balanced reaction which requires the addition of water into the system. The exact stoichiometry depends on the exact compositions of the minerals which are not available.

$$Czo + Hbl + H_2O \rightarrow Pmp + Chl + Qz \qquad \text{(Eq. 1.)}$$

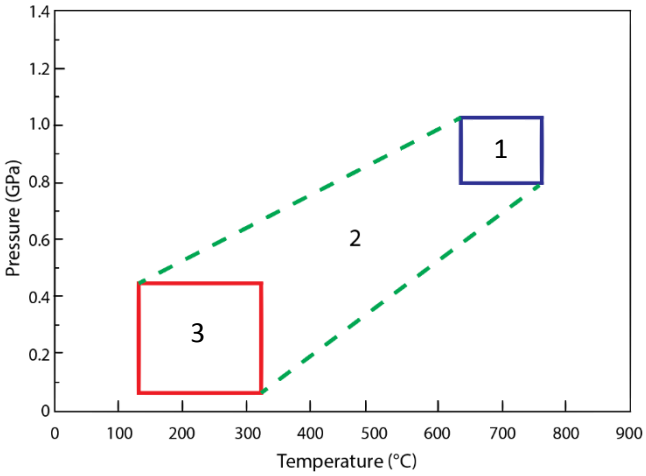

Fig. 13. Suggested chain of events pertaining to fault formation and metamorphism. 1) Formation of coherent amphibolite. 2) Shearing and opening of fault. 3) Pumpellyite crystallization.

Using the data presented above, a non-unique list of steps constraining the timing of fault formation and subsequent metamorphism is suggested (Fig. 13). The coherent amphibolite formed at 114.5 Ma (Anczkiewicz et al., 2004) at amphibolite facies pressures and temperatures. The coherent amphibolite then experienced shearing and opening to form the fault. The opening would have allowed for the influx of mélange matrix material, and shearing would have broken off hornblende grains into the incoming mélange matrix. This suggested timing of events assumed contemporaneous shearing and opening, allowing for fault material mixing and thus producing the geochemical heterogeneity of the fault. It is during this time that the chlorite and hornblende clasts in the fault experienced differential stress and folds, fractures, and kinked grains were developed. Finally, the crystallization of pumpellyite (and quartz and chlorite) from hornblende, clinozoisite, and water occurs, suggesting a potential increase in water entering the system and potentially retrograde metamorphism.

8. Conclusions

1) The Cottonwood Canyon fault zone developed through a combination of shearing and opening.

2) Geochemical heterogeneity and deformation microstructures of the fault imply that the fault formed by shearing of host amphibolite and mixing with the mélange matrix during opening of the fault.

3) Microstructural and petrological observations place constraints on the sequence of events for the formation of the Cottonwood Canyon fault, which are as follows: the amphibolite crystallized, followed by deformation (shearing and opening of the fault), followed by pumpellyite

crystallization. The pressure and temperature conditions during which the deformation took place are unclear.

4) Evidence of a chemical reaction producing pumpellyite indicates some form of retrograde metamorphism.

5) The more ultramafic nature of the fault rock and damage zone made apparent by higher Os, Ir, and Ru concentrations as compared to the host amphibolite implies that the mélange matrix was at some point mobile and capable of flowing into other systems outside of its own.

9. Acknowledgments

I would like to thank Dr. Sarah Penniston-Dorland, Dr. Melodie French, and Dr. Richard Walker for their tireless efforts in training me in the field and lab and to answer my streams of questions. I would also like to thank Dr. Stanley A. Mertzman for collecting the XRF data at Franklin and Marshall College, the Catalina Island Conservancy for their permission to conduct field work, and the Department of Chemistry at the University of Maryland for collecting XRD spectra. The research was funded by National Science Foundation grant EAR-141987.

10. References

Anczkiewicz, R., Platt, J.P., Thirlwall, M.F., Wakabayashi, J., 2004. Franciscan subduction off to a slow start: evidence from high-precision Lu-Hf garnet ages on high grade-blocks: Earth and Planetary Science Letters, v. 225, p. 147-161.

Bebout, G.E., 2007. Metamorphic chemical geodynamics of subduction zones: Earth and Planetary Science Letters, v. 260, p. 373-393.

Bebout, G.E. and Barton, M.D., 1989. Fluid flow and metasomatism in a subduction zone hydrothermal system: Catalina Schist terrane, California: Geology, v. 17, p. 976-980.

Bebout, G.E. and Barton, M.D., 2002. Tectonic and metasomatic mixing in a high-T, subduction-zone mélange – insights into the geochemical evolution of the slab – mantle interface: Chemical Geology, v. 187, p. 79-106.

Bebout, G.E. and Penniston-Dorland, S.C., 2016. Fluid and mass transfer at subduction interfaces – The field metamorphic record: Lithos, v. 240-243, p. 228-258.

Becker, H. et al., 2001. Rhenium-osmium systematics of calcium-aluminum-rich inclusions in carbonaceous chondrites: Geochimica et Cosmochimica, v. 65, p. 3379-3390.

Becker, H. et al., 2006. Highly siderophile element composition of the Earth's primitive upper mantle: Constraints from new data on peridotite massifs and xenoliths: Geochimica et Cosmochimica Acta, v. 70, p. 4528-4550.

Boulton, C. et al., 2017. Geochemical and microstructural evidence for interseismic changes in fault zone permeability and strength, Alpine Fault, New Zealand: Geochemistry, Geophysics, Geosystems, v. 18, p. 238-265.

Brown, E.H., 1977. Phase equilibria among pumpellyite, lawsonite, epidote and associated minerals in low grade metamorphic rocks: Contributions to Mineralogy and Petrology, v. 2, pg. 123-136.

Chester, F.M., Evans, J.P., and Biegel, R.L., 1993. Internal Structure and Weakening Mechanisms of San Andreas Fault: Journal of Geophysical Research, v. 98, p. 771-786.

Gieré, R. and Sorensen, S.S., 2004. Allanite and Other REE-Rich Epidote-Group Minerals: Reviews in Mineralogy and Geochemistry, v. 56, p. 431-493.

Greenwood, H.J., 1963. The Synthesis and Stability of Anthophyllite: Journal of Petrology, v. 4, p. 317-351.

Hirth, G. and Tullis, J., 1991. Dislocation creep regimes in quartz aggregates: Journal of Structural Geology, v. 14, p. 145-159.

Liou, J.G., Maruyama, S., Cho, M., (1985). Phase equilibria and mineral parageneses of metabasites in low grade-metamorphism: Mineralogical Magazine, v. 49, p. 321-333.

Pennison-Dorland, S.C., Gorman, J.K., Bebout, G.E., Piccoli, P.M., Walker, R.J., 2014. Reaction rind formation in the Catalina Schist: Deciphering a history of mechanical mixing and metasomatic alteration: Chemical Geology, v. 384, p. 47-61.

Penniston-Dorland, S.C., Walker, R.J., Pitcher, L., Sorensen, S.S., 2012. Mantle-crust interactions in a paleosubduction zone: Evidence from highly siderophile element systematics of eclogite and related rocks: Earth and Planetary Science Letters, v. 319-320, p. 295-306.

Platt, J.P., 1975. Metamorphic and deformational processes in the Franciscan Complex, California: Some insights from the Catalina Schist terrane: Geological Society of America Bulletin, v. 86, p. 1337-1347.

Shipton et al., 2006. How Thick is a Fault? Fault Displacement-Thickness Scaling Revisited: Earthquakes: Radiated Energy and the Physics of Faulting, v. 170, p. 193-198.

Sorensen, S.S., 1988. Petrology of amphibolite facies mafic and ultramafic rocks from the Catalina Schist, southern California: metasomatism and migmitization in a subduction zone metamorphic setting: Journal of Metamorphic Petrology, v. 6, p. 405-435.

Sorensen, S.S. and Barton, M.D., 1987. Metasomatism and partial melting in a subduction complex: Catalina schist, southern California: Geology, v. 15, p. 115-118.

Sorensen, S.S. and Grossman, J.N., 1989. Enrichment of trace elements in garnet amphibolites from a paleo-subduction zone: Catalina Schist, Southern California: Geochimica et Cosmochimica Acta, v. 53, p. 3155-3178.

Whitney, D.L. and Evans, B.W., 2010. Abbreviations for names of rock-forming minerals: American Mineralogist, v. 95, p. 185-187.

Appendix I: Osmium and HSE Separation Methods

For initial digestion and Os separation, samples are mixed with spikes, put into Pyrex Carius tubes with concentrated HCl, and put into a bucket of ice. Concentrated HNO_3 is added and the Carius tubes are placed in ice again. Once sealed, the Carius tubes are placed in a sealed jacket with a copper gasket and placed into a 220-240°C oven. Each sample requires a 15 mL Teflon container and a 60 mL centrifuge tube that have been cleaned, rinsed, dried, and labeled with the appropriate sample number. Each sample is designated three 5 mL pipette tips, labeled "acid," "solvent," and with the respective sample number. Three mL of carbon tetrachloride solution (CCl_4) is added to each centrifuge tube. Four mL of concentrated HBr is added to each Teflon container. The Carius tubes are frozen, opened, and thawed, and contents are poured into the centrifuge tubes which are then placed in the centrifuge for one to three minutes. With the designated sample pipetter tip, CCl_4 is pipetted from the bottom of the centrifuge tube into the Teflon containers containing the HBr. Three mL of CCl_4 is added to the centrifuge tube and centrifuged again. The CCl_4 is removed from the centrifuge tube and placed into the Teflon containers and this step is repeated once more. The pipetter tips are then rinsed and saved for later use. The sealed Teflon containers are placed on an 85°C hotplate for at least two hours but no longer than overnight. Once cooled, the CCl_4 is extracted from the bottom of the Teflon container and placed in a waste bottle. The Teflon container is then placed below a heat lamp where the HBr dries until it is about a 40 µL droplet. Caps and bottoms of 5 mL conical bottom Teflon vials are labeled for each sample. With a clean 50-200 µL pipetter tip, 40 µL of HBr is removed from the 15 mL Teflon container and placed in the flat cap, which is then placed under a heat lamp, and capped once dry.

Once the above process is completed, the now-dry Os sample is ready for micro-distillation. Fifteen µL of concentrated HBr is placed in the tip of a 5 mL conical bottom Teflon vial cap, ensuring that all of the HBr is at the bottom. About 20-30 µL of dichromate solution is added to the flat cap containing the dried Os sample. The cap containing the Os and dichromate is screwed onto the vessel containing the HBr, ensuring that the HBr is not shaken from the top. Remaining inverted, the closed vessel is wrapped in aluminum foil and put on an 85°C hot plate for two to three hours. Following this, the Teflon container is removed from the hot plate and the aluminum foil is removed. Milli-Q (MQ) H_2O is added to the residue to ensure that the distillation was a success; upon MQ addition to the residue, a resultant yellow color indicates successful distillation, whereas a green color indicates insufficient Cr^{+3} ions are oxidizing Os, and that more dichromate needs to be added and the sample redistilled. Once the cap is placed back on the sample, the container containing the HBr rests for a few hours to ensure all of the Os is reduced. Finally, the HBr and Os is placed under a heat lamp to evaporate the HBr, after which the Os left behind is loaded onto a clean filament and analyzed via TIMS.

Left behind from the Os separation is the aqua regia and "sludge" which is centrifuged in a 50 mL centrifuge tube for about 5-10 minutes at maximum speed. The aqua regia is then pipetted into the 15 mL Teflon container used previously for the Os separation, and the sludge is placed in acid waste containers. The centrifuge tubes are then rinsed and saved. Once placed under a heat lamp, aqua regia in the 15 mL Teflon tube is dried until very viscous (almost, but not completely, solid). To remove all HNO_3 and lower the normality of the HCl, 2.5-10 mL of 1 N Teflon distilled HCl is added to the Teflon container and placed on the hot plate. The sample is then placed under the heat lamp to partially dry the sample, and then the step of adding HCl and partially drying is repeated once more. Finally, about 2.5 mL of 1N Teflon distilled HCl is placed into the Teflon

container and back onto the hot plate at around 80-90° to completely dissolve the sample. At this point the sample is prepared for column chemistry and chromatography.

In order to conduct the column chemistry and chromatography, cleaned, rinsed, and labeled Biorad 2 mL disposable columns are placed in a column stand with drip cups below. About 1.7 mL anion resin is pipetted into each column. Once the water from the resin drips out, the column and resin can be cleaned. Five mL of MQ H_2O is pipetted into each column and drained, followed by 10 mL of concentrated quartz distilled (QD) HNO_3, 10 mL of concentrated Teflon distilled (TD) HNO_3, 2 mL of MQ H_2O, 10 mL of QD concentrated HCL, 2 mL of MQ H_2O, 2 mL of 1N TD HCl, and 2 mL of 1N TD HCl. After this process, the samples can be loaded into the columns. Once the samples are loaded into the columns, two 6 mL rounds of 1N TD HCL + HF are pipetted into the columns, followed by two 2 mL rounds of 0.8N TD HNO_3. At this point Re and Ru are collected in a cleaned and labeled 15 mL Teflon container by pipetting 12 mL of 6N TD HNO_3. In another cleaned and labeled 15 mL Teflon container, Pt and Ir are collected by pipetting 13 mL of concentrated TD HNO_3 followed by 2 mL of MQ H_2O. Finally, in a third cleaned and labeled 15 mL Teflon container, 14 mL of concentrated TD HCl is pipetted into the column. Once all samples are collected, they are dried separately and completely under a heat lamp, making sure to avoid sample splattering.

To more thoroughly clean the Re + Ru samples, the dried Re + Ru sample is re-dissolved in 0.5 mL 1N TD HCl on an 80˚C hotplate for at least one hour. A 0.25 mL column that has been cleaned and rinsed in MQ H_2O is placed in a column stand with clean AGIx8 anion resin within 0.5 cm of reservoir base with drip cups below column. Eluted are 2 mL MQ H_2O, followed by 10 mL concentration TD HNO_3, 1 mL MQ H_2O, and two rounds of 2 mL 1N TD HCL. The re-dissolved Re + Ru sample is loaded into the column, followed by two rounds of 1 mL TD HCL and two rounds of 1 mL 0.8N TD HNO_3. In order to collect the Re + Ru, 7 mL 6N QD HNO_3 is put into the column and collected in a 15 mL Savillex container. Two to three drops of concentrated TD HCl and HNO_3 are added to the beaker containing the Re + Ru sample and dried to remove any organics.

It is at this point that all dried HSE samples are ready to be put into solution for ICP-MS analysis. Fifty μL of concentrated HNO_3 are added to samples in Teflon containers at least an hour prior to ICP-MS analysis except for Pd samples. Pd samples should be put into solution as close to analysis as possible as it may be adsorbed into the plastic of the Teflon container once mixed with the HNO_3. Each sample then gets 950 μL of MQ H_2O, and the dissolved sample is transferred to a clean and labeled 1.5 mL centrifuge tube from which the solution is analyzed via ICP-MS.

A blank can be produced and analyzed to quantify how much of the measured HSE concentrations were contributed to the samples from outside sources. This is simply done by mixing spikes in a separate Teflon vessel without any sample and following the above procedures. The data collected from the spike can be used to calculate the uncertainties of the data: The reported uncertainty for HSE concentrations is the percentage of blank contribution. $^{187}Os/^{188}Os$ ratio uncertainty is reported as two standard error. $^{187}Re/^{188}Os$ ratio uncertainty is reported as the percentage of blank contained within the Re sample prior to blank correction and $^{187}Os/^{188}Os_{initial}$ ratio uncertainty is reported as the change in ratio if uncertainty from the $^{187}Re/^{188}Os$ ratio is considered. The age used to calculate $^{187}Os/^{188}Os_{initial}$ is 114.5 Ma, which was used by Penniston-Dorland et al. (2012) to calculate $^{187}Os/^{188}Os_{initial}$ of mafic blocks. This age of the coherent amphibolite was determined by Anczkiewicz et al. (2004).

Appendix II: Detailed Rock Descriptions

Sample Name	*Lithologic Unit (Transect)*	*Hand Sample Description*	*Dominant Microstructures*	*Grain Size (mm)*	*Mineralogy*
A16-01A	Fault rock (1)	Unconsolidated, fine-grained, distinctly green	--	--	--
A16-01B	Fault rock (1)	Somewhat unconsolidated, fine- to medium-grained, radial crystals, distinctly green	Transgranular and intragranular fractures	0.5-15	Pmp+yellow material+Ttn
A16-01C	Fault rock (1)	Somewhat unconsolidated, fine- to very coarse-grained, distinctly green, prominent fracturing	Transgranular and intragranular fractures, intragrain offset (~1 mm), fabric and granular folding	<1-15	Pmp+Ttn+yellow material
A16-02	Fault rock (1)	Coarse-grained, somewhat linearly oriented grains	Transgranular and intragranular fractures, slightly deformed/folded grains	<0.5-30	Hbl+Ep+Pl+Qz+Ttn
A16-03	Fault rock (1)	A) Somewhat unconsolidated, prominent folding, medium-grained (~1 cm), B) Incoherent, fine-grained	Transgranular and intragranular fractures, folding, distinct zones of different mineralogies and grain sizes	0.5-8	Hbl+Pl+Qz+yellow material+Ttn
A16-04	Coherent amphibolite (1)	Coarse-grained, linear orientation, large vein (~3-5 mm thick), slight folding (~3-4 cm)	Transgranular and intragranular fractures, veins	<0.5-10	Hbl+Pl+Ep++Ttn+Zrn
A16-05	Coherent amphibolite (1)	Coarse-grained, quartz/plagioclase boudins (~1-2 cm), folding (~1-2 cm)	Intragranular fractures, veins, folding, somewhat distinct zones of different mineralogies and grain sizes, intragrain offset (~1 mm)	<0.5-10	Hbl+Qtz+Pl+Ep+Chl
A16-06	Coherent amphibolite (2)	Somewhat unconsolidated, coarse-grained, veins (~1-8 mm)	Transgranular and intragranular fractures, veins	0.5-60	Hbl+Pl+Qtz
A16-07	Fault rock (2)	Somewhat unconsolidated, coarse- to very coarse-grained, slight folding (~2.5 cm), prominent fractures, distinct green amphibole crystals	Intragranular fractures, veins	<0.5-60	Hbl+Cl+Pl+Ep+red oxide
A16-08a (hand sample)	Fault rock (2)	Unconsolidated, mostly medium-grained, distinct fine-grained white monomineralic portion	--	--	--
A16-08a (thin section)	Fault rock (2)	Somewhat unconsolidated, medium- to very coarse-grained, distinct fine-grained white monomineralic portion, slight folding (~3 cm)	Transgranular fractures, folding	<0.5-10	Chl+Hbl+Ep+red oxide
A16-08b (thin section)	Fault rock (2)	[See A16-08a (thin section)]	Intragranular fractures, intragrain offsets (~2 mm), kinked grains	<0.5-30	Chl+Hbl+red oxide+Ep+Ttn
A16-09	Fault rock (2)	Moderately unconsolidated, medium-grained, quartz/plagioclase boudins (~3 mm-2 cm)	Transgranular fractures, pinched grains	<0.5-9	Hbl+Qtz+Pl+Chl+red oxide+Ttn+Rt+Aln
A16-10	Coherent amphibolite (2)	Coarse-grained, somewhat linear orientation of grains	Transgranular and intragranular fractures, folding	<0.5-35	Hbl+Pmp+Pl+Rt+red oxide
A16-11	Fault rock (2)	Unconsolidated, very fine-grained, monomineralic, distinctly white	--	--	--
A16-12	Coherent amphibolite*	Coarse-grained, linear orientation of grains	Intragranular fractures	0.5-10	Hbl+Ep+Ttn+Aln+red oxide
A16-13	Fault rock (3)	Very-fine grained, prominent fracturing	Transgranular and intragranular fractures, folding, kinked grains	<0.5-9	Chl+Ep+Ttn+red oxide
A16-14	Fault rock (3)	Very fine-grained, prominent fracturing	Transgranular fractures	<0.5-5	Chl+Ep+red oxide
A16-15	Coherent amphibolite (3)	Very coarse-grained, some fractures, slight folding (~5 cm), linear orientation of grains	Transgranular and intragranular fractures, vein	2-40	Hbl+Ep
A16-16	Coherent amphibolite (3)	Coarse-grained, quartz/plagioclase boudins (~2 mm-2 cm) and veins (~1-2 mm thick), linear orientation of grains, very slight folding (~2 cm)	Intragranular fractures, intragrain offsets (~4 mm)	1-60	Hbl+Ep+Pl+Ttn

Table AII *Table format similar to that of Boulton et al. (2017). The mineral abbreviations are those found in Whitney and Evans (2010): Ep – epidote, Hbl – hornblende, Pl – plagioclase, Pmp – pumpellyite, Ttn – titanite, Qz – quartz, Zrn – zircon. *Sample not part of transect; collected 64 m away from fault but considered a representative of undeformed/unaltered host amphibolite.*

Appendix III

Black spectra were obtained via XRD; colored spectra were closest matches of mineral XRD spectra. All samples are fault rock from transect 2. a) Sample A16-08 contains magnesiohornblende. b) Sample A16-08a contains actinolite. c) Sample A16-011 contains pumpellyite.

A

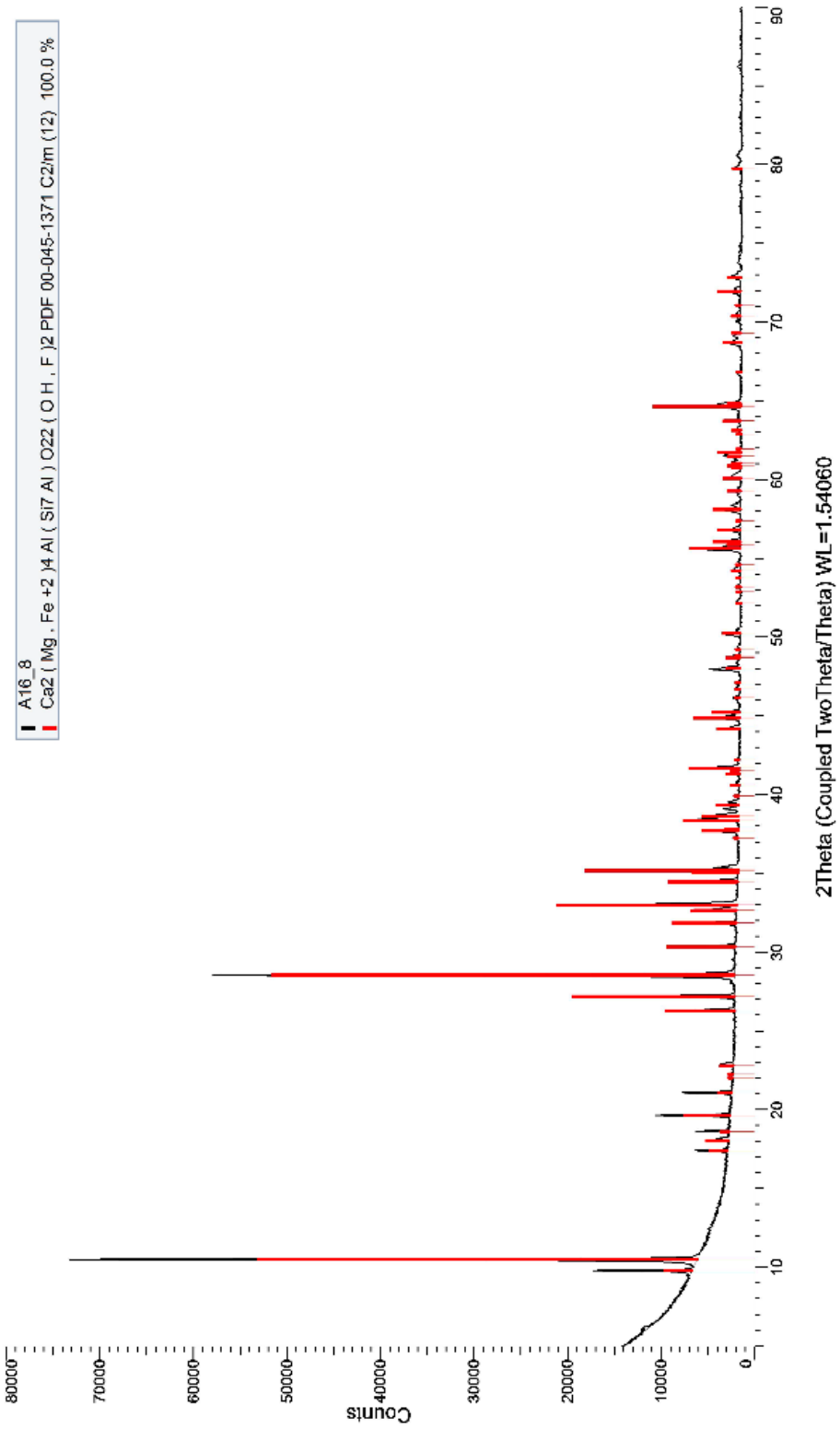

B

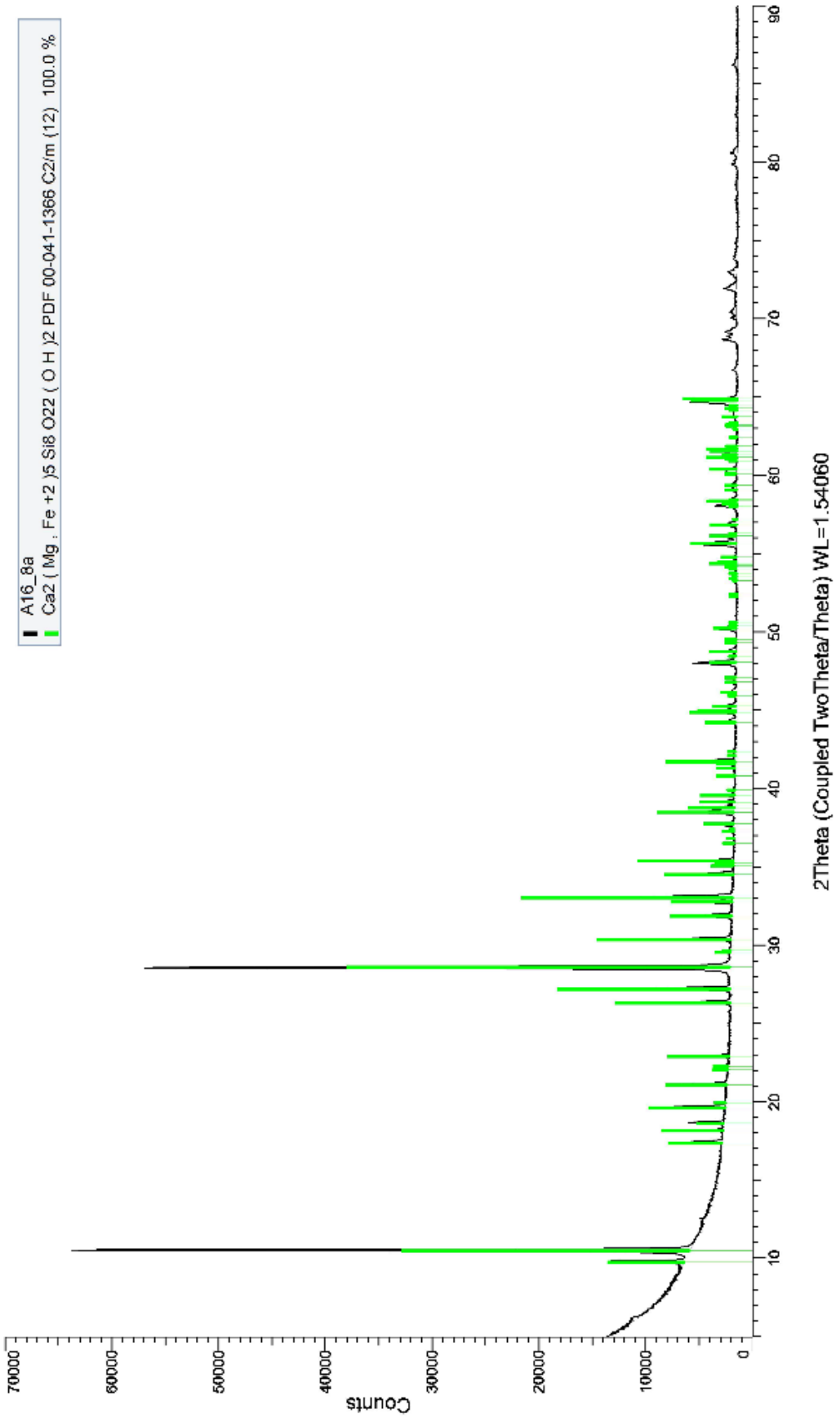
A16_8a
Ca2 (Mg , Fe +2)5 Si8 O22 (O H)2 PDF 00-041-1366 C2/m (12) 100.0 %
Counts
70000
60000
50000
40000
30000
20000
10000
0
10
20
30
40
50
60
70
80
90
2Theta (Coupled TwoTheta/Theta) WL=1.54060

C

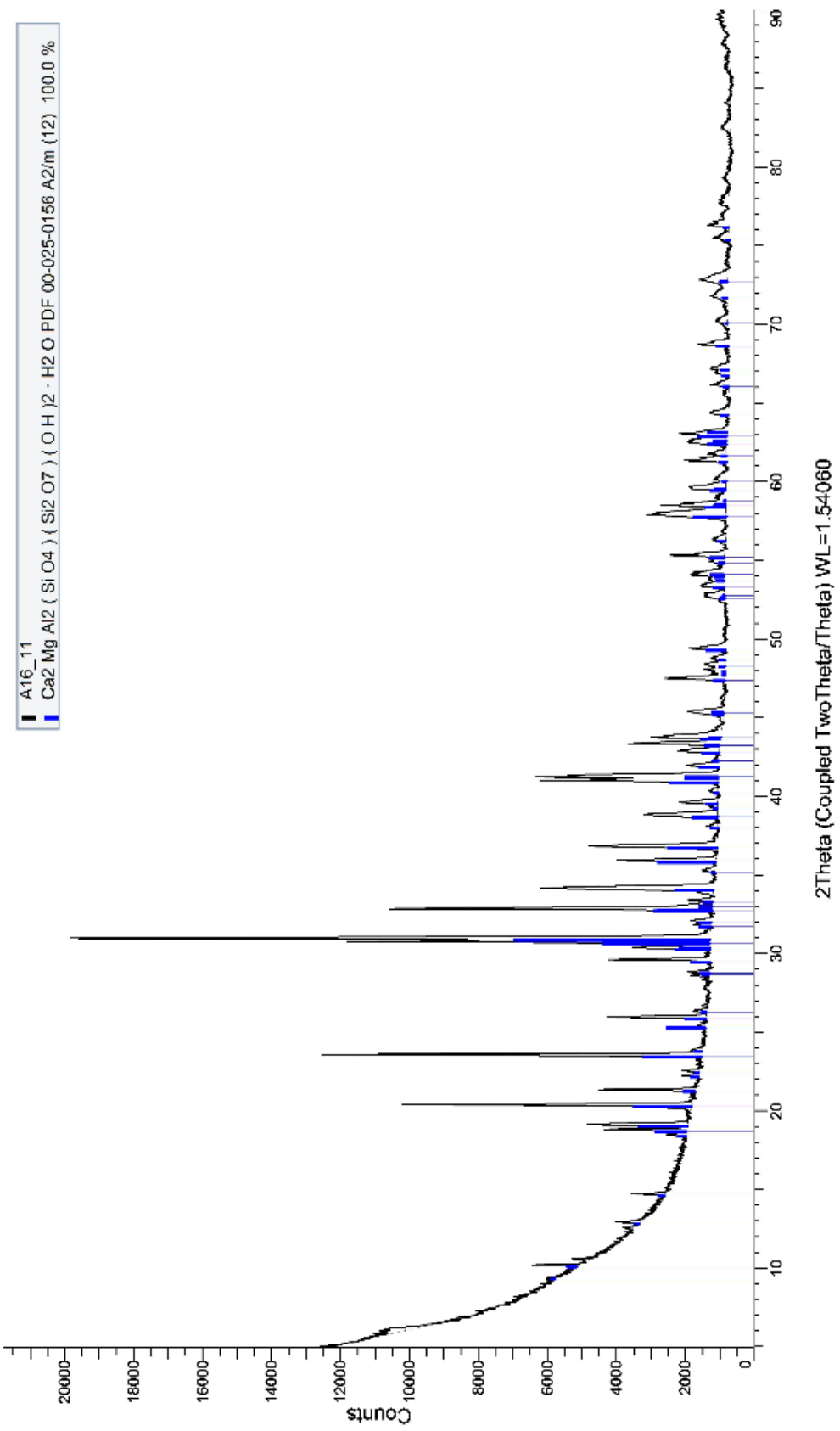
A16_11
Ca2 Mg Al2 (Si O4) (Si2 O7) (O H)2 · H2 O PDF 00-025-0156 A2/m (12) 100.0 %
Counts
2Theta (Coupled TwoTheta/Theta) WL=1.54060
0
2000
4000
6000
8000
10000
12000
14000
16000
18000
20000
10
20
30
40
50
60
70
80
90

Appendix IV: Honor Code

I pledge on my honor that I have not given or received any unauthorized assistance or plagiarized on this assignment.

_____

Justine Giovanna Grabiec